Scalable High-Efficiency Multilayered Anti-icing/de-icing Coating: Superhydrophobic Upper Layer Boosts the Performance of the Electrothermal System

Yanbei Hou, Mingqing Wang, Kwang-Leong Choy*

Institute for Materials Discovery, University College London, London, United Kingdom, WC1E 7JE

*Corresponding author. Tel/Fax: +44 (0)20 7679 1335. E-mail address: k.choy@ucl.ac.uk.

Abstract: The formation and accumulation of ice can easily cause serious safety issues and damage. The superhydrophobic surface can delay ice formation due to its liquid repellence feature, but does not work very well under super cold temperatures. The electrothermal coating can effectively prevent ice formation, while it is very energy-consuming. In this work, a multilayered system that combined electrothermal layer (ET) with energy-saving superhydrophobic layer (SH) (SH@ET system) was fabricated to improve the energy efficiency of anti-icing/de-icing coatings. A programmable automatic spraying machine was used to prepare the graphene nanoplates (GNP)-based electrothermal coating with controllable electrical resistance and excellent electrothermal performance. After spraying the SH layer, the SH@ET coating showed excellent water repellency, superior anti-icing performance, and extremely low ice adhesion strength (15 kPa). During the anti-icing test, there was no ice accumulation on the surface of assembled SH@ET system even under low power (0.5 W) at -19°C for 20 min, confirming its practical application prospects. The SH@ET system also exhibited

superior deicing performance than the ET coating. An obvious difference appeared at the low applied voltage range, under which ice continuously formed on the surface of ET coating, while no ice formed on the SH layer. The results can be ascribed to the better water repellency and low ice adhesion strength of the SH layer. This work provides a feasible approach for designing multilayer anti-/de-icing systems for practical large-area applications.

Keywords: Electrothermal; Superhydrophobic; Multilayered system; Anti-icing; Deicing.

1. Introduction

The formation and accumulation of ice can easily cause serious damage to facilities such as power lines, aircraft engines, and wind turbines [1]. At present, deicing methods are classified into active deicing and passive deicing according to the working mechanisms [2]. The active method refers to deicing by an external force after freezing, including mechanical, salt, electrothermal, infrared, and other deicing methods [3, 4], which require certain energy or resources. The passive method refers to the use of the coating to prevent water from condensing or to reduce the ice adhesion strength (τ_{ice}) [5, 6]. This method relies on wind or gravity to get the ice off the surface. However, traditional mechanical and thermal technologies with high energy consumption are far from reaching the requirements of energy-saving and lightweight design. Meanwhile, current passive systems are not sufficient for complete and long-term protection from icing problems. Theoretically, the integration of active and passive systems will combine the advantages of individual coatings and exhibit desirable performance. There is literature that has reported electrothermal coating-based anti-/de-icing systems, which are

mainly focused on the functionalization of electrothermal coating [7, 8]. However, there are not many articles studying the influence of the upper layer on the overall anti-icing performance of the multi-layered electrothermal coating.

Electrothermal layer is a widely used active de-icing method to raise the temperature of the substrate, thereby preventing freezing or melting of the ice [9, 10]. Recently, to improve de-icing performance and decrease the energy consumption of the electrothermal layer, carbon nanotubes (CNTs) and graphite-based coating were investigated intensively, due to their high conductivity and high steady-state heating temperature [11, 12]. These carbon materials can convert electric energy to heat with high efficiency [13], which makes them good candidates for next-generation electrothermal coatings. Graphene nanoplate (GNP), as two-dimensional carbon allotropes, has been the focus of mass investigation in electrothermal fields due to its record high thermal conductivity and superior electronic mobility [14, 15]. Previous studies have demonstrated that graphene-based polymer nanocomposites can be fabricated as highly conductive electrical conductors [16]. However, the practical strategy for preparing GNP-based anti-icing coating has been rarely reported. The main reason is that achieving desirable de-icing performance needs high voltage (> 30 V)[3, 17, 18]. In addition, the resistance of the heating layer cannot be adjusted accurately with these coatings, which is also a reason why it cannot be used at large-scale. Therefore, it is necessary to fabricate an electrothermal layer with low and adjustable electric resistance.

For passive anti-icing layers, superhydrophobic surfaces have been intensively investigated in the anti-icing field. The large-value (> 150 °) contact angle with water

(CAW) reduces the contact area between the droplet and the superhydrophobic surface, resulting in a decrease in heat transfer efficiency, and finally delaying the freezing time [19, 20]. Meanwhile, due to the small rolling angle, water droplets are difficult to stay on the surface of the coating, thereby, less water/ice accumulates on the surface. It is to be noted that a superhydrophobic layer cannot stop ice accumulation in an extremely cold environment. Because water vapor will form a capillary bridge between the droplet and the superhydrophobic layer, promote heat transfer, and eventually cause ice [21, 22]. If there is a strategy to prevent the forming of the capillary bridge, the anti-icing performance of the superhydrophobic layer will be further improved. The key of which is to improve the surface temperature of the superhydrophobic layer.

Based on the discussion and justification above, the superhydrophobic coating upper layer was integrated with the electrothermal layer underneath to form an anti-icing/de-icing system. The effect of the upper layer on the anti-icing/de-icing performance of the SH@ET coating was investigated. Poly(vinylidene fluoride-*co*-hexafluoropropylene) (PVDF-HFP) with high solvability, hydrophobicity and suitable mechanical strength was selected as the polymeric matrix for the electrothermal and superhydrophobic layers. GNP-based electrothermal coating and SiO_2/carbon nanotubes (CNTs)-based superhydrophobic coating were prepared by automatic spraying method. The construction of a multilayered system is illustrated in Figure 1. The insulating layer is only used when the substrate is a conductive material. Conductive copper tapes are used to connect to the power supply. Automatic spraying equipment is assembled by a 3D printer and an airbrush kit as shown in Figure 1a.

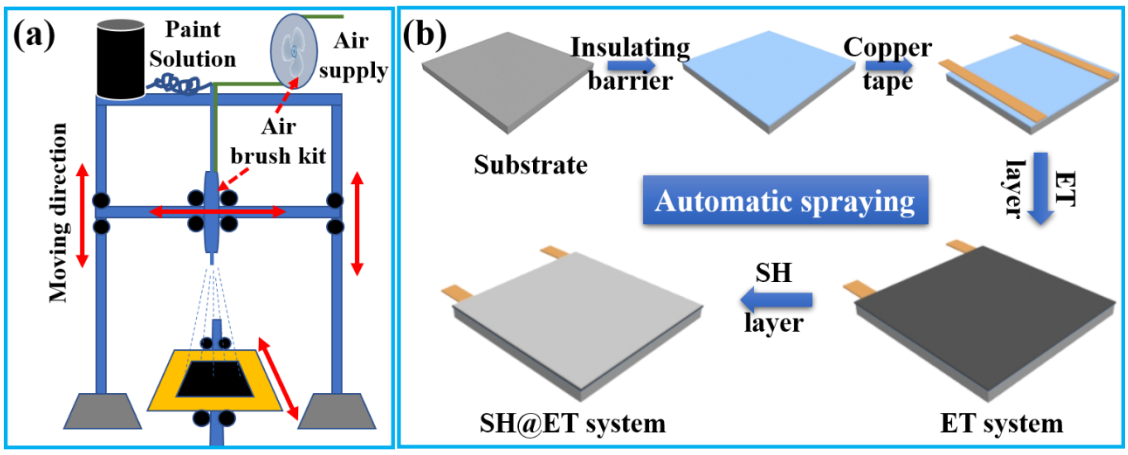

Figure 1. (a) Illustration of the automatic spraying equipment ; (b)preparation processes of anti-/de-icing system.

2. Experimental

2.1 Materials

PVDF-HFP (pellet, average Mw ~400,000), dimethylformamide (DMF), GNP (25 μm particle size, surface area 50-80 m^2/g), and SiO_2 (nanopowder, 10-20 nm particle size) were purchased from Sigma-Aldrich. Perfluorosiloxane was bought from Fluorochem company (United Kingdom). Acidized CNTs (TNDC, -COOH; Outer diameter 2-4 nm; Length ~50μm) were purchased from TimesNano (Chengdu, China).

2.2 Preparation of electrothermal solution

PVDF-HFP (0.1 g) was dissolved in 10 mL DMF with vigorous stirring at room temperature. After PVDF-HFP was dissolved completely, 0.05 g GNPs was added into the solution and ultrasonicated for 1.5 h to obtain a homogeneously dispersed GNPs solution.

2.3 Preparation of superhydrophobic solution

Generally, PVDF-HFP (0.34 g) was dissolved in 10 g DMF by vigorous stirring at room

temperature. Then nanosized SiO_2, acidized CNTs and certain perfluorosiloxane were added into the solution. With the assistance of an ultrasonic probe, an ink-like solution can be obtained. The weight ratio of polymer, CNTs, and SiO_2 is 1:0.02:0.5. Acidized CNTs are used in this work to immobilize SiO_2 nanoparticles, which will increase the integrity of coating, and thus improve the abrasion resistance of the rigid surface [23].

2.4 Preparation of multilayered system

Both synthesized solutions can be used as paint to prepare anti-/de-icing coatings by spraying, brushing ,and dipping methods. In order to make the sample thickness adjustable and to make the spraying process efficient, we designed and built programmable automatic spraying equipment, which is shown in Figure 1a. All samples were prepared by this automatic spraying machine in this work. The movable hot plate moves in the X-axis, and the spray gun moves with Y-axis. The Z-axis is used to adjust the distance between spray gun and substrate, based on the spray speed and the evaporation speed of the solvent. In this work, the distance was fixed at 17 cm above the 80°C hot plate. The moving speed of the spray gun is 60 mm/s. Stainless steel sheets are selected as substrates due to their widespread usage in industry. A commercial primer paint (Halfords Etch Primer 500 ml, insulting barrier in Finger 1b) was pre-coated on the steel substrate to increase its adhesion strength with ET coatings. As shown in Figure 1b, commercial insulating paint was sprayed on the surface of stainless steel first, and then the electrothermal layer was fabricated by automatic spraying. Superhydrophobic solution was deposited on the ET layer to form a SH@ET anti-/de-icing system. All samples tested in this work are 5 cm × 5 cm in size on stainless steel sheets.

2.5 Characterization

A scanning electron microscopy (SEM) (Evo LS15, Zeiss, UK) was used to characterize the surface morphology of the fabricated nanocomposite coating. Sessile contact angles and bounce test were measured by optical tensiometer from Biolin Specific One Attention® Theta Contact Angle Optical Tensiometer' goniometer, dropping ~3μL of deionized water onto a substrate. The water bounce test was also conducted by this equipment. The needle was placed 2 cm above the sample and produced ~3μL water droplets. Thermogravimetric analysis (TGA) was carried out using a Perkin-Elmer 2000 instrument, under continuous nitrogen flow of 70 mL/min, and A 10 mg sample was used and the weight loss was recorded from 30 to 700 °C with temperature ramp at 20 °C/min. A 250 g loading was applied to the coatings, and 1200 grid 3M sandpaper was used as the abrading surface. According to ASTM D3359-02 standard, the sandpaper reciprocated on the surface of the sample. To test the impact influence on SH coating, a water flow of 30 mL/s was washed against the SH surface vertically from a height of 5 cm. The anti-icing test was performed in a -19^{o}C freezer (the humidity: 57.2%) equipped with a transparent door. Measurement of ice adhesion strength was performed using a vertical motorized test stand MX2-500N (IMADA Co., Ltd, Japan). Ice adhesion strength(τ_{ice}) was calculated through the adhesion strength divided by the contact area of ice columns with the sample surface. To determine the de-icing performance of ET, a piece of purpose-built equipment consisting of a freezer, a digital-control DC power supply, and a timer has been assembled. De-icing time (t_d) is recorded as the time taken for the ice to slip or rotate from the coating surface under certain electrothermal power. Custom setups were

designed and conducted to investigate the robustness of as-synthesized superhydrophobic coating. Detailed information can be found in related sections.

3. Results and discussion

3.1 Surface morphologies of multi-layer systems

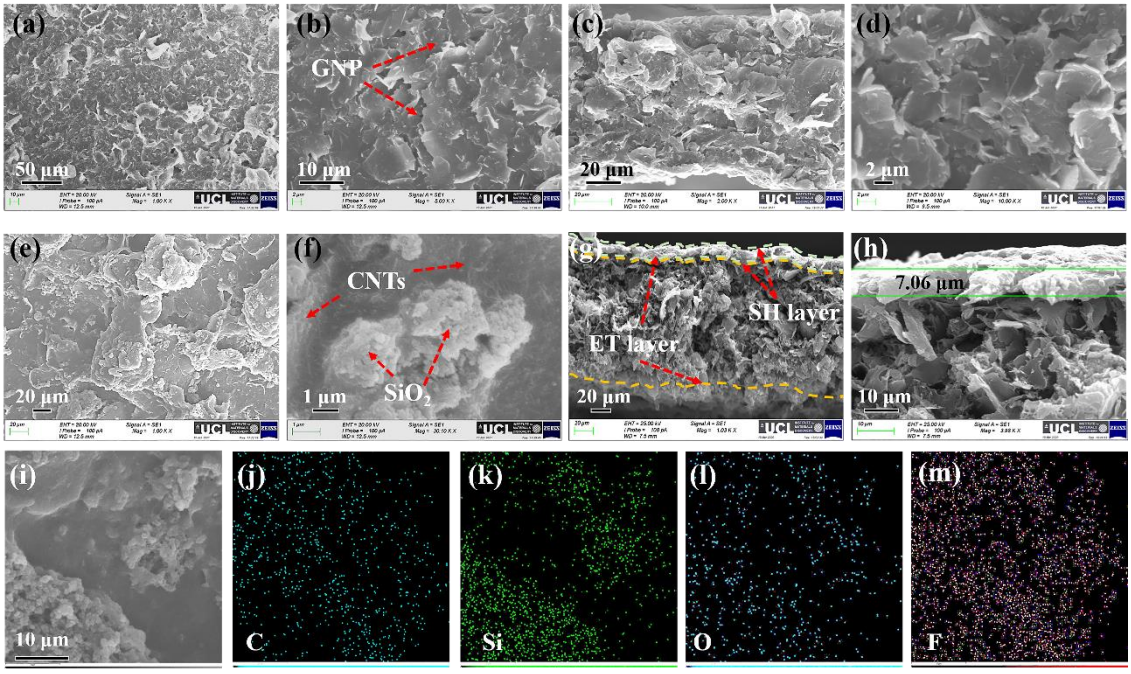

Figure 2. SEM images of surface (a, b) and fractured section (c, d) of ET coating with different magnification; SEM images of SH surface (e, f); Fractured surfaces of SH@ET nanocomposite coating (g, h); EDS mapping image of SH surface (i-m).

Surface morphologies of as-synthesized samples were observed by SEM, results shown in Figure 2. GNP sheets are embedded in the polymeric matrix and form a rough surface (Figure 2a). Overlapped GNP provided a well conductive route for ET samples (Figure 2b), which is beneficial for preparing conductive layers with controllable electric resistance. The morphology of the fractured section of the ET layer shows the stacked way of GNP (Figure 2c and d). Randomly dispersed GNP overlapped layer by layer to

form a continuous pathway for charge transport. SH layer shows a different morphology with ET layer, with hill-like structures of different sizes decorated on the surface of the SH layer (Figure 2e). In an amplified view we can see, the micro-structured lump was composed of long CNTs and sphere SiO_2 nanoparticles (Figure 2f). It has been reported that this lotus-like structure contributes superhydrophobicity to coatings by providing surface roughness and decreasing surface free energy [24]. The fracture surface of an integrated system composed of the ET layer and SH layer is shown in Figure 2g. It can be seen that there is a clear boundary between the two layers, but no obvious separation is observed. The same polymeric matrix is used as an adhesive agent to improve the compatibility of these two different layers. The ultrathin upper layer can be seen in Figure 2h, the thickness of which was less than 10 μm. The SH layer functions as a super-hydrophobic coating and insulating layer here. The CNTs used in this work are acidified and the concentration of which is low (< 1.3 wt%), which makes SH layer electrical insulation. The resistance of the SH layer exceeds the maximum range of the multimeter (200 MΩ). When a voltage of 30 V is applied, no current is detected. Both results confirmed that no conductive path was formed in the SH layer, resulting in an electrically insulating coating. The elemental distribution of C, Si, O, and F in Figure 2i-m confirmed the agglomerated SiO_2 nanoparticles and well-dispersed polymeric matrix (acting as a binder).

3.2 Thermostability of layers

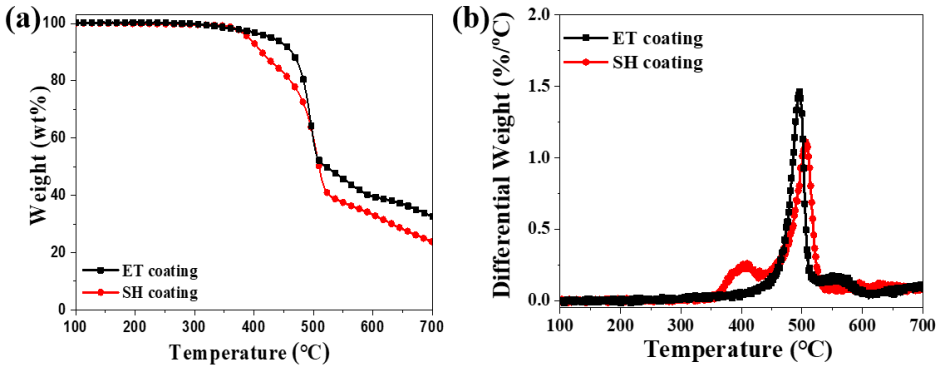

Figure 3. (a) TG and (b) DTG curves of ET and SH layers.

Thermostability plays a significant role in the application of polymer composites. TGA is an effective measurement to determine the thermal stability of materials [25]. The TG curves of the as-deposited nanocomposite coatings are shown in Figure 3a. The weight loss of the ET and SH layer would begin at circa 400°C, indicating they have excellent thermal stability. Compared with the ET layer, the initial decomposition (5 % weight loss) temperature of the SH layer (at 391°C) is lower than that of ET layer (at 430°C), which can be ascribed to the degradation of low molecular compounds in fillers, such as water and perfluorosiloxane. The maximum degradation rate can be studied from differential thermogravimetric (DTG) curves in Figure 3b. The maximum degradation rate of all samples occurred at a temperature above 300°C, which is high enough for heating purposes, indicating that both samples have good thermostability.

3.3 Conductive and electrothermal properties of ET layer and its system

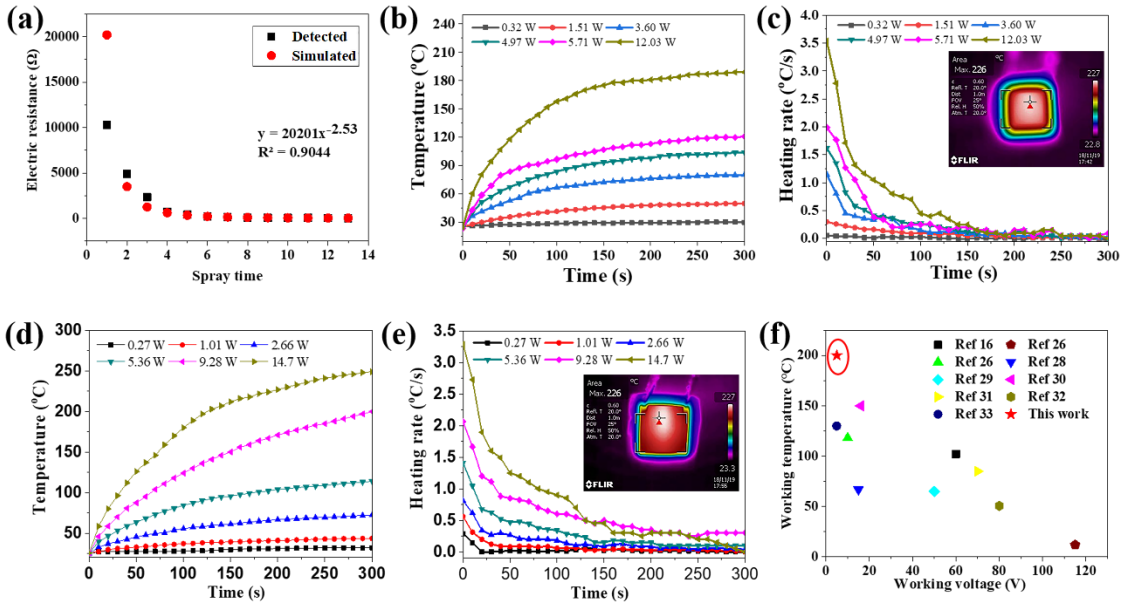

Figure 4 (a)The relation between spray time and electrical resistance of the ET coating; (b, c) Electrothermal properties of the ET coating and (d, e) SH@ET system under varied heating power; (f) Comparisons of electrothermal performance between previous paper and this work [16, 18, 26-32].

An interesting phenomenon observed is that there is a defined relationship between thickness and resistance. The resistance of samples was adjusted by increasing or decreasing the thickness of the ET layer. The automatic spraying machine and homogeneous ET solution were applied to investigate this relationship, as shown in Figure 4a. A power correlation between electric resistance and spray time (thickness) was found. In order to obtain low resistance, the thickness of the ET layer should reach the threshold value. In this work, we prepared ET samples with varied resistance (from 5 to 70 Ω) by controlling the thickness (from 60 to 42 μm) of the coating. The result is highly consistent with the simulated data. The current electrothermal system used for de-icing is mainly limited by its huge energy consumption (voltage > 30 V). Preparing a low-voltage

and high-performance electrothermal layer is a key to promoting the application of these materials. In this work, we applied a low external power with a maximum voltage of 11 V. Compared with previous research, it is relatively low. Considering the equation $1/R_t=1/R_{ET} + 1/R_{SH}$, where R_t denotes total resistance, while R_{ET} and R_{SH} denote resistances of ET layer and SH layer, respectively. Since the value of R_{SH} (insulation, >200 MΩ) is much larger than R_{ET} (~20 Ω), we can conclude that the SH layer has no effect on the value of R_t and electrical conductivity of the ET layer.

Figure 4 shows the time-temperature curves (Figure 4b, d) and heating rate curves (Figure 4c, e) of the ET coating and SH@ET system. The lower the resistance of the sample is, the higher power can be obtained at the same voltage. As shown in Figures 4b and d, the highest steady-state heating temperature increases with increasing applied power. However, to protect polymeric components in samples, all experiments stopped at circa 250ºC. Considering the equation $P = U^2/R$ (where P is power, U is the applied voltage, and R is the resistance) and higher resistance, ET coating displays a lower steady-state temperature and lower heating rate at the same applied power, compared with the SH@ET system. Another reason is that the existence of the SH layer reduces the heat transfer between the ET layer and the air, thereby reducing heat radiation, so that the SH@ET system shows a higher heating rate. Heating rate is an important factor to estimate the electrothermal performance of samples. It is obvious that the heating rate increased with the increase of power (Figure 4c and e). Electrothermal layers can reach high temperatures at low voltage. The infrared thermal images of the ET coating and SH@ET system at 226ºC under different applied powers. It should be noted that the

temperature distribution of ET coating and SH@ET system at the applied powers is rather homogeneous. This even distribution of heat may be attributed to the excellent thermal and electrical conductivity of GNPs as well as the highly uniform surface of the ET coating and SH@ET system. Compared with previous reports, ET coating fabricated in this work can reach the highest temperature at lower working voltage, as shown in Figure 4f. The size of the samples fabricated using the spray deposition process outlined here is not limited to small sizes. Thus, it is possible to scale up the systems for applications that require larger active areas.

3.4 Water repellency of coatings

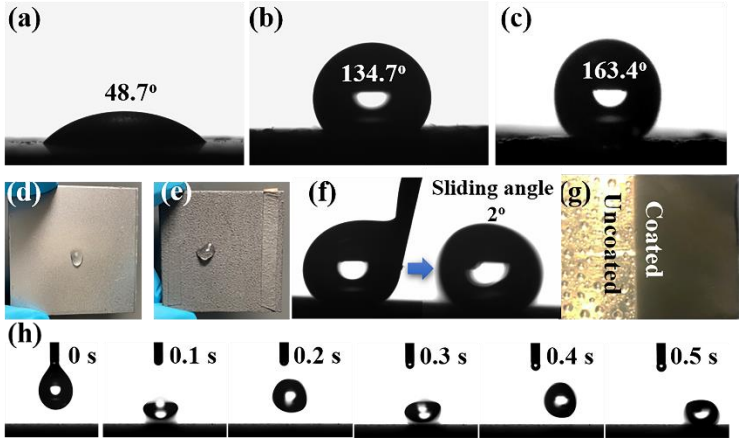

Figure 5. Water contact angle test of: (a) steel; (b) ET layer; (c) SH coating; Water droplet affinity test of: (d) steel; (e) ET coating; (f) water roll away from SH coating with 2° sliding angle; (g) Water mist test of SH coating; (h) Video process of droplet bounces up and down from the surface of SH layer.

Stainless steel shows good hydrophilicity and has a small water contact angle (CAW) (48.7°), which is much lower than that of ET coating (134.7°) (Figure 5a and b). The fluorine-rich polymer and hydrophobic GNPs led to a good water repellency to ET layer.

Droplet on the surface of SH coating keeps its spherical shape and the value of CAW is over 163°, indicating the superhydrophobicity of the SH coating (Figure 5c). The roll-off angle, at which a drop rolls off from the inclination surface, is about 2° of the SH layer. The low roll-off angle shows excellent water repellency of the SH coating layer. Stainless steel and ET coating show excellent water affinity, that is, water droplets can be firmly attached on their surface even placed in a vertical position, as shown in Figure 5d and e. It stands in sharp contrast to the SH layer, on which water droplets would roll off from the surface even at a very small angle (2°) (Figure 5f). Water mist, produced by household water can, is sprayed onto uncoated and coated Al substrate, as shown in Figure 5g. No small droplet is seen on the SH surface, while big droplets reunited by water mists scatter on the surface of the uncoated substrate, indicating excellent water repellency of the SH coating. As shown in Figure 5h, a water droplet bounces off the SH surface with extremely low adhesive force at 2° inclination. All results above confirm superhydrophobicity and excellent water repellency of the SH coating. Less water accumulated on the surface of SH layer denotes less ice would form consequently.

3.5 Robustness of ET and SH coatings

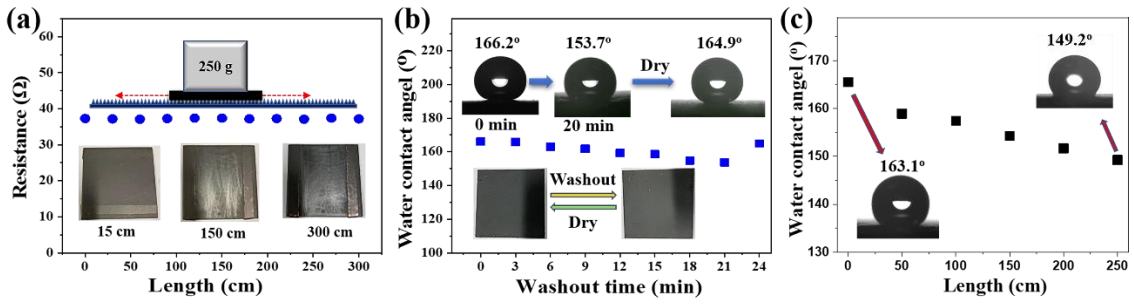

Figure 6 (a) Anti-wear test of ET coating; (b) water impact test of SH layer; (c) anti-wear test of SH coating.

A schematic view of the abrasion test is shown in Figure 6a. The ET coating was rubbed reciprocated for 3 meters on the surface of sandpaper, leaving clear but not deep friction marks. After the abrasion, the electric resistance of the ET sample was retested and nearly no change was found, indicating the robustness of the nanocomposite coating. The phenomenon can be ascribed to the proven excellent self-lubrication of GPN [33]. The robustness of the SH coating is also demonstrated by a water impact test. A water flow with a flow rate of 30 mL/s was ejected toward the SH surface vertically from 5 cm above the coating, as shown in Figure 6b. The water stayed on the SH surface for a short time and was quickly squeezed down by the subsequent water flow. It can be observed that air separated water and SH surface, reducing the direct contact between them. After continuous flush with high-speed water (15 mL/s), the value of WCA of SH coating decreased from 166.2^{o} to 153.7^{o} within 21 min. However, the WCA of SH coating increased to 164.9^{o} after drying, indicating the SH layer regained most of its superhydrophobicity. Under constant water flow, the humidity of the environment for coating is extremely high. Small-size droplets or moisture infiltrate into the voids among nano-/micro-structures, thus increasing the water affinity of the SH layer. However, when the infiltrated water is removed by evaporation, the water repellency/superhydrophobicity of the SH coating can be regained. The recovery of the superhydrophobic property can be attributed to the fact that water impact didn't damage the micro/nanostructure of the SH surface, thereby water-repelling property is maintained. The mechanical stability of the SH layer was tested by sandpaper in the same conditions as the ET layer. As shown in Figure 6c, the superhydrophobicity of the SH coating remained unchanged even after a 2

m length of abrasion. Therefore, it can be concluded that both ET coating and SH coating exhibited good robustness.

3.6 Anti-icing performance of coatings

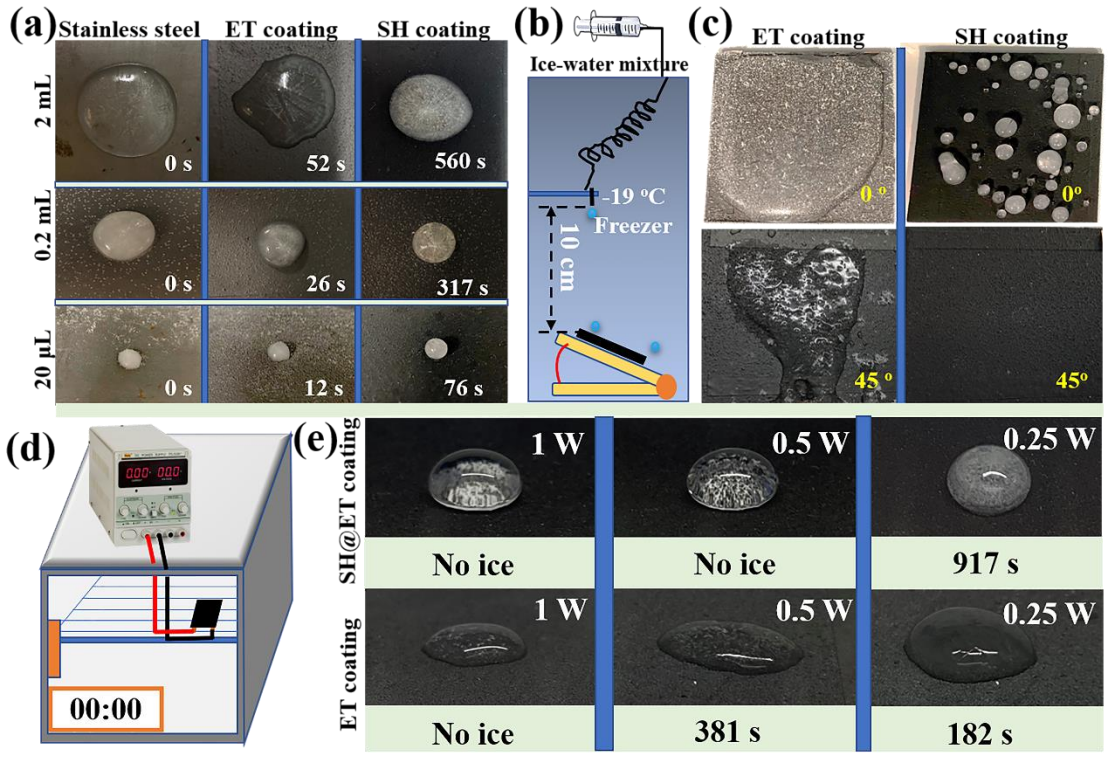

Figure 7. Anti-icing tests of fabricated nanocomposite coatings: (a) Icing time with different volume of water; (b) Illustration of anti-icing test setup; (c) Digital images taken after the anti-icing test with different angles of inclination; (d) Illustration of anti-icing test with power supply; (e) Digital images during the anti-icing test under different power.

To compare the anti-icing performance of all coatings, we designed three different anti-icing tests at -19°C, simulating typical application scenarios in cold regions. The influence of the volume of water on the anti-icing performance of nanocomposite coatings was first investigated, and the result was shown in Figure 7a. All samples were cooled to -19°C

before test and the icing time of droplet on stainless steel was recorded as starting time. In cold conditions, water droplets still kept their spherical structure on the SH surface, while water spread over the surface of steel and ET coating. It is clear that the larger the droplet, the longer the icing time. The anti-icing performance of SH coating is excellent, compared with uncoated steel. The ice forming process of 2mL droplet on SH coating was delayed by circa 560 seconds. Large ice crystals can be observed on the SH surface, while transparent or semi-transparent ice was formed on uncoated steel and ET layer. This phenomenon can be ascribed to the poor thermal transport situation of droplets on the insulating SH surface, which leads to a slow icing process and larger ice crystals [34]. In our previous study, we found that the setting position of samples also influences the anti-icing performance of coatings. A purpose-built anti-icing test equipment is designed as shown in Figure 7b. When samples were placed horizontally, water droplets (5 g) gathered on the surface of the ET layer and no water rolled away from the surface. In contrast, most water (3.22 g) droplets bounced away from the SH surface, leaving some spherical water droplets on the SH surface (Figure 7c). At a 45^{o} inclination angle; almost half of water (2.41 g) was removed from the surface of the ET layer. As seen from Figure7c, ice was still accumulated on the surface of the ET layer. Distinct from water/ice adhesion on ET layer, no water remains on the surface of SH layer at inclination angle as low as 30^{o} due to the excellent water repellency property of SH layer at low temperature.

In order to prevent ice accumulation on the surface in the freezer, the ET coating must continue to operate under external heating power, which would cause a lot of energy consumption. Figure 7d shows the anti-icing test of the ET sample and SH@ET sample

with heating power on, and the results are shown in Figure 7e. When the heating power was 1 W (4.5 V) or higher, there was no ice accumulated on the surface of both samples. However, when the heating power decreased to 0.5 W, the water droplet finally turned into ice after 381 s on ET coating, while large water droplets on SH coating kept at liquid state even after 1200 s. The icing time of droplet on ET coating decreased to 182 s when the heating power was 0.25 W. Whereas, it took 917 s to make the droplet totally turn into ice. From the results in Figure 7e, it can be seen the anti-icing performance of both ET and SH@EH coatings is obviously improved with the increase of the heating power. There is a synergy advantage by integration of ET and SH coatings, that is, the presence of the SH layer decreased the required heating power to prevent ice accumulation on the ET surface, and the Joule heat generated by the ET layer further delayed the icing time of droplet on the SH coating. Therefore, it is an excellent strategy to combine these two layers together to reduce ice hazards.

3.7 Adhesion strength and de-icing performance of coatings

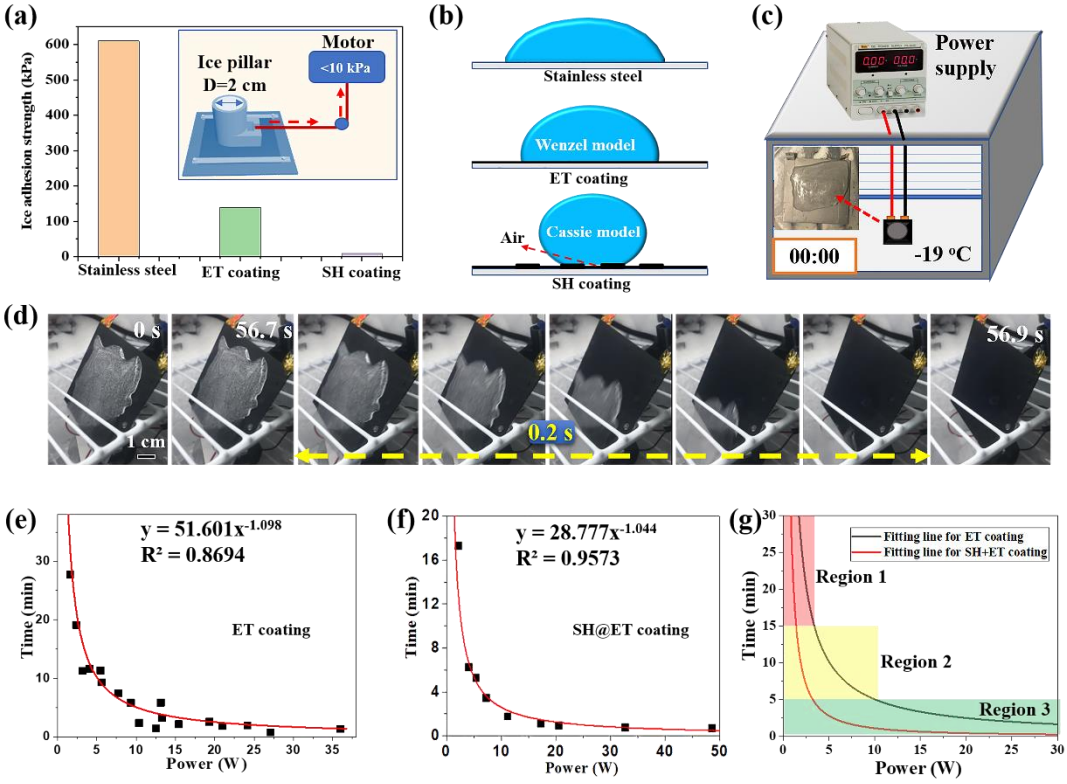

Figure 8. (a) Ice adhesion strength of samples; (b) Illustration of droplet-substrate interfaces; (c)Pictures of the purpose-built anti-icing test setup; (d) Photos of the moment of ice slip; (e, f)The deicing time (t_d) of ET and SH@ET coatings under different power; (g)Comparisons between two fitted t_d-power curves.

Ice adhesion strength(τ_{ice}) is an important factor to compare the anti-icing properties of different coatings. Adhesion strength of SH samples prepared in this work was extremely low (τ_{ice}= 15 kPa, as shown in Figure 8a) compared with ET coating (147 kPa) and untreated stainless steel (610 kPa) due to icephobicity of the SH coating. Moreover, the water impact test has little effect on the τ_{ice} value of SH coating, ranging from 15 to 24 kPa. The relatively low τ_{ice} obtained from this work, indicated the designed SH@ET coating shows great potential as a high-efficiency anti-icing/de-icing system [35-37]. These desirable results can be mainly attributed to the fact that the water droplet has a

smaller contact area on the SH coatings than that of uncoated substrates. A smaller contact area between ice and SH coating contributes to a smaller τ_{ice} value. The surface of the SH layer is composed of micro/nano structures. SiO_2 nanoparticles and their agglomeration lead to the presence of both microstructures and nanostructures in the composite. The low ice adhesion strength of the SH layer is due to the existence of large air pockets trapped by these micro/nano structures and hydrophobic fluorinated substances. An impregnating contact model (Wenzel model) is formed when water droplet deposits on the microstructured surface, which leads to stronger ice adhesion at low temperature due to the mechanical interlocking of ice. However, a spherical water droplet (Cassie model) is formed on the hybrid micro/nanostructured surface. The suspended water droplet in Cassie mode resulted in a layer of air between the ice and micro/nanostructured surface, which further leads to the lower ice adhesion strength. In addition, the water layer at the ice/hydrophobic surface interfaces near water frozen temperature could act as a lubricating layer and thus decrease the ice adhesion strength. To determine the de-icing performance of ET, a piece of purpose-built equipment consisting of a freezer, a digital-control DC power supply, and a timer has been assembled, as shown in Figure 8c. To keep the comparability of the experimental data, 5 g water was cooled to form ice on the surface of each coating. As soon as ice-slipping or ice-rotation happened under heating power, we recorded the time as de-icing time (t_d). Figure 8d gives a glimpse of de-icing process of the SH@ET coating system. The related videos comparing the deicing performance of ET and SH@ET coatings were provided in the supplementary files. After turning on the power, the ice near the coating surface rapidly melts within 60 s under the action of Joule

heat, turning the solid-solid interface of the ice-matrix into a solid-liquid-solid interface. The SH coating with excellent superhydrophobicity greatly weakens the two-phase adhesion, thereby melting ice can slip away from the surface of multi-layer coating faster, just as shown in the videos.

As shown in Figure 8e, it is obvious that t_d is greatly dependent on the applied power. As soon as ice-slipping or ice-rotation happened, the time would be recorded as t_d. It is interesting to observe that at low heating power (P < 1W), water is difficult to turn into ice on the ET surface. While once ice is formed, it cannot be melted. As the power increases, the deicing time decreases sharply and then stabilizes. The SH@ET system exhibits similar de-icing performance as ET coating, but with smaller t_d than ET coating under the same heating power (Figure 8f). At the highest power (48 W), it is to be noted that ice on the surface of SH@ET system can be removed in less than 60 s, demonstrating its practicability in the de-icing field. In figure 8g, the de-icing efficiency of coatings was classified into three levels based on the deicing time, that is difficult (region 1, t_d > 15 min), medium (region 2, 5 min < t_d < 15 min) and easy (region 3, t_d < 5 min). In Figure 8g, both fitting curves for the relationship between time of deicing and heating power show a similar tendency, that is, the higher the heating power, the less time is needed to de-ice. However, the relationship between deicing time and power is not a linear relationship, but a power relationship. The presence of the SH layer pushes the curve closer to the axis and the origin point, denoting it takes less time for the assembled SH@ET system than the ET layer to remove the same amount of ice. Obviously, to achieve easy deicing coating in region 3, it requires 3 W of heating power for the SH@ET

system and about 10W for the ET coating. A 70% decrease of the required power supply to achieve the same deicing time directly confirms the vital role of the SH layer in this de-icing system. Based on above analysis we can conclude that the top SH layer boosts deicing performance of the electrothermal layer and has a promising application prospect in cold regions.

4. Conclusions

This work successfully deposited ET coatings with controllable electrical resistance and thickness and SH@ET anti-icing/de-icing systems by a purpose-built automatic spraying machine. The fabricated ET coating can reach a high stable temperature of 226ºC at low voltage (8 V) with a fast-heating rate. The deposited SH layer has little adverse effect on the performance of the ET layer, but it can significantly improve the anti-icing/de-icing performance of the ET coating. Compared with the pure ET layer, the icing time of the droplet on SH@ET coating was dramatically delayed from 26 s to 317 s. Furthermore, even a small inclination angle can prevent the formation of ice on the SH coating, but the ET coating does not have such performance. Furthermore, the presence of the ET layer improves anti-icing performance of the SH layer. Even at low heating power ($P \geq 0.5$ W), droplets cannot form ice on the SH@ET system, which is superior to ET coating. It can be attributed to the Joule heat generated by the ET layer that removes the moisture absorbed between the droplet and the polymer matrix, which not only transfers heat from the substrate to the droplet, but also cuts off the heat transfer from the droplet to the substrate, thereby preventing ice forming. Meanwhile, the deposition of the SH layer dramatically reduced the ice adhesion strength of the ET de-icing coating. Compared with

ET coating, the SH@ET system shows less de-icing time and requires lower heating power, demonstrating the high de-icing efficiency with low energy consumption. This work has demonstrated a multilayered anti-/de-icing system, which can be applied to address icing problems in extremely cold conditions, which has practical applications and added value and significance for energy-saving anti-/de-icing technologies.

Acknowledgement

This research was funded by the European Commission (SEDNA: Safe maritime operations under extreme conditions: the Arctic case, project 723526).

References

[1] C.C. Ryerson, Ice protection of offshore platforms, Cold Regions Science and Technology, 65 (2011) 97-110.

[2] T. Wang, Y. Zheng, A.-R.O. Raji, Y. Li, W.K. Sikkema, J.M. Tour, Passive anti-icing and active deicing films, ACS applied materials & interfaces, 8 (2016) 14169-14173.

[3] Y. Sun, X. Sui, Y. Wang, W. Liang, F. Wang, Passive anti-icing and active electrothermal deicing system based on an ultraflexible carbon nanowire (CNW)/PDMS biomimetic nanocomposite with a superhydrophobic microcolumn surface, Langmuir, 36 (2020) 14483-14494.

[4] X. Yin, Y. Zhang, D. Wang, Z. Liu, Y. Liu, X. Pei, B. Yu, F. Zhou, Integration of self-lubrication and near-infrared photothermogenesis for excellent anti-icing/deicing performance, Advanced Functional Materials, 25 (2015) 4237-4245.

[5] L. Cao, A.K. Jones, V.K. Sikka, J. Wu, D. Gao, Anti-icing superhydrophobic coatings, Langmuir, 25 (2009) 12444-12448.

[6] Y. Long, X. Yin, P. Mu, Q. Wang, J. Hu, J. Li, Slippery liquid-infused porous surface (SLIPS) with superior liquid repellency, anti-corrosion, anti-icing and intensified durability for protecting substrates, Chemical Engineering Journal, 401 (2020) 126137.

[7] M. Zhang, S. Zhan, Z. He, J. Wang, L. Wang, Y. Zheng, J. Liu, Robust electrical uni-directional de-icing surface with liquid metal (Ga90In10) and ZnO nano-petal composite coatings, Materials & Design, 126 (2017) 291-296.

[8] Y. Liu, R. Xu, N. Luo, Y. Liu, Y. Wu, B. Yu, S. Liu, F. Zhou, All-Day Anti-Icing/De-Icing Coating by Solar-Thermal and Electric-Thermal Effects, Advanced Materials Technologies, (2021) 2100371.

[9] F. Pinto, F. Ciampa, M. Meo, U.J.S.M. Polimeno, Structures, Multifunctional SMArt composite material for in situ NDT/SHM and de-icing, 21 (2012) 105010.

[10] Z. Wang, Y. Zhu, X. Liu, Z. Zhao, J. Chen, X. Jing, H. Chen, Temperature self-regulating electrothermal pseudo-slippery surface for anti-icing, Chemical Engineering Journal, 422 (2021) 130110.

[11] D. Sui, Y. Huang, L. Huang, J. Liang, Y. Ma, Y.J.S. Chen, Flexible and transparent electrothermal film heaters based on graphene materials, 7 (2011) 3186-3192.

[12] T. Kawano, H.C. Chiamori, M. Suter, Q. Zhou, B.D. Sosnowchik, L. Lin, An electrothermal carbon nanotube gas sensor, Nano letters, 7 (2007) 3686-3690.

[13] R. Menzel, S. Barg, M. Miranda, D.B. Anthony, S.M. Bawaked, M. Mokhtar, S.A. Al-Thabaiti, S.N. Basahel, E. Saiz, M.S.J.A.F.M. Shaffer, Joule Heating Characteristics of Emulsion-Templated Graphene Aerogels, 25 (2015) 28-35.

[14] A.K. Geim, Graphene: status and prospects, science, 324 (2009) 1530-1534.

[15] Q. He, S. Wu, Z. Yin, H. Zhang, Graphene-based electronic sensors, Chemical Science, 3 (2012) 1764-1772.

[16] N. Karim, M. Zhang, S. Afroj, V. Koncherry, P. Potluri, K.S. Novoselov, Graphene-based surface heater for de-icing applications, RSC advances, 8 (2018) 16815-16823.

[17] T. Hao, Z. Zhu, H. Yang, Z. He, J. Wang, All-day anti-icing/deicing film based on combined photo-electro-thermal conversion, ACS Applied Materials & Interfaces, 13 (2021) 44948-44955.

[18] P. Wang, T. Yao, Z. Li, W. Wei, Q. Xie, W. Duan, H. Han, A superhydrophobic/electrothermal synergistically anti-icing strategy based on graphene composite, Composites science and technology, 198 (2020) 108307.

[19] L. Wang, Q. Gong, S. Zhan, L. Jiang, Y. Zheng, Robust anti-icing performance of a flexible superhydrophobic surface, Advanced Materials, 28 (2016) 7729-7735.

[20] Y. Lin, H. Chen, G. Wang, A.J.C. Liu, Recent progress in preparation and anti-icing applications of superhydrophobic coatings, 8 (2018) 208.

[21] F. Wang, C. Li, Y. Lv, F. Lv, Y. Du, Ice accretion on superhydrophobic aluminum surfaces under low-temperature conditions, Cold regions science and technology, 62 (2010) 29-33.

[22] N. Wang, D. Xiong, Y. Lu, S. Pan, K. Wang, Y. Deng, Y. Shi, Design and fabrication of the lyophobic slippery surface and its application in anti-icing, The Journal of Physical Chemistry C, 120 (2016) 11054-11059.

[23] S. Kulinich, S. Farhadi, K. Nose, X. Du, Superhydrophobic surfaces: are they really ice-repellent?, Langmuir, 27 (2011) 25-29.

[24] Z. Wei, W. Liu, D. Tian, C. Xiao, X. Wang, Preparation of lotus-like superhydrophobic fluoropolymer films, Applied Surface Science, 256 (2010) 3972-3976.

[25] Y. Hou, W. Hu, Z. Gui, Y. Hu, Preparation of metal–organic frameworks and their application as flame retardants for polystyrene, Industrial & Engineering Chemistry Research, 56 (2017) 2036-2045.

[26] J.-w. Hong, J.H. Jung, S.-m. Yong, Y.-r. Kim, J. Park, S.J. Lee, J.-h. Choi, Radio-frequency transparent carbon nanotube electrothermal film for radome de-icing application, Journal of Materials Research and Technology, 9 (2020) 10854-10862.

[27] Y. Ibrahim, R. Kempers, A. Amirfazli, 3D printed electro-thermal anti-or de-icing system for composite panels, Cold Regions Science and Technology, 166 (2019) 102844.

[28] H. Ba, L. Truong-Phuoc, T. Romero, C. Sutter, J.-M. Nhut, G. Schlatter, G. Giambastiani, C. Pham-Huu, Lightweight, Few-Layer Graphene Composites with Improved Electro-Thermal Properties as Efficient Heating Devices for De-Icing Applications, Carbon, (2021).

[29] X. Yao, S.C. Hawkins, B.G. Falzon, An advanced anti-icing/de-icing system utilizing highly aligned carbon nanotube webs, Carbon, 136 (2018) 130-138.

[30] F. Wang, B. Yang, Z. Zhang, Q. He, Y. Zhang, Synergistic effect of hybrid fillers on electro-thermal behavior of nanocomposite for active de-icing application, Composites Communications, 25 (2021) 100746.

[31] S.-M. Yong, S.J. Lee, J. Park, J. Hong, J.H. Jung, Y. Kim, Fiber-reinforced plastic material with de-icing capability for radome application, Materials Letters, 284 (2021) 128943.

[32] F. Zangrossi, F. Xu, N. Warrior, P. Karapappas, X. Hou, Electro-thermal and mechanical performance of multi-wall carbon nanotubes buckypapers embedded in fibre reinforced polymer composites for ice protection applications, Journal of Composite Materials, 54 (2020) 3457-3469.

[33] G. Ren, Z. Zhang, X. Zhu, B. Ge, F. Guo, X. Men, W. Liu, Influence of functional graphene as filler on the tribological behaviors of Nomex fabric/phenolic composite, Composites Part A: Applied Science and Manufacturing, 49 (2013) 157-164.

[34] S. Kono, M. Kon, T. Araki, Y. Sagara, Effects of relationships among freezing rate, ice crystal size and color on surface color of frozen salmon fillet, Journal of food engineering, 214 (2017) 158-165.

[35] G. Zhang, Q. Zhang, T. Cheng, X. Zhan, F. Chen, Polyols-infused slippery surfaces based on magnetic Fe3O4-functionalized polymer hybrids for enhanced multifunctional anti-icing and deicing properties, Langmuir, 34 (2018) 4052-4058.

[36] G. Momen, R. Jafari, M. Farzaneh, Ice repellency behaviour of superhydrophobic surfaces: Effects of atmospheric icing conditions and surface roughness, Applied Surface Science, 349 (2015) 211-218.

[37] X. Liu, H. Chen, Z. Zhao, Y. Yan, D. Zhang, Slippery liquid-infused porous electric heating coating for anti-icing and de-icing applications, Surface and Coatings Technology, 374 (2019) 889-896.